Large-area quantification of subaerial CO_2 anomalies with portable laser remote sensing and 2D tomography

Manuel Queißer[1], Mike Burton[1], and Domenico Granieri[2]

Abstract

Quantifying subaerial fluxes of CO_2 is key in a diverse range of applications, including carbon capture and storage sites, emissions from urban areas and industrial sites such as oil refineries, or forecasting volcanic eruptions. All of these have one thing in common: they represent spatially extended sources with a generally unknown spatial distribution of CO_2 concentration. The conventional approach to measure CO_2 fluxes is to first measure CO_2 concentrations in situ at several points and estimate 2D CO_2 concentration profiles. Along with the plume transport speed, the concentration profiles can then be used to compute CO_2 fluxes. Active remote sensing of CO_2 concentrations offers crucial advantages over in situ probing, including a spatially comprehensive measurement, a safe measurement distance, and faster acquisition, which enables real-time monitoring. This makes it also a viable complement or alternative to fence-line monitoring at industrial sites. In the last few years, technology has advanced sufficiently to allow for the realization of robust and portable remote sensing platforms that are relatively inexpensive and user friendly. Within the frameworks of the European Research Council CO_2Volc and proof-of-concept CarbSens projects, such a remote sensing platform has been developed to probe CO_2 emissions. It may be operated from a fixed location on the ground, from moving platforms (e.g., cars), or be airborne. The kit was used to probe CO_2 concentrations and perform a feasibility test to obtain a tomographic 2D image of the subaerial CO_2 distribution inside the Solfatara crater, part of arguably the most hazardous volcano in the world: Campi Flegrei near Naples, Italy. The methodology could be applied directly to industrial applications, including quantifying fugitive CO_2 at storage and industrial sites. An unmanned aerial vehicle portable kit is envisaged.

Introduction

Climate prediction models rely on accurate and spatially well-resolved inputs of CO_2 surface sources and sinks in the form of fluxes (emission rates). Growing urban areas represent significant sources of excess CO_2, mainly from traffic and industrial sites, and thus an input of increasing importance to these models. In reality, CO_2 flux maps are still rather scarce and, especially at local scales, CO_2 sources are not well resolved in terms of their overall strength and origin (e.g., human versus natural source strength). With platforms such as NASA's Orbiting Carbon Observatory 2, satellite remote sensing is now able to provide high-resolution (~2 km grid) maps of CO_2 concentrations, which helps meet this demand. However, satellite-based remote sensing is currently passive, i.e., relying on sunlight, so it is restricted to lower latitudes (Amediek et al., 2008), daytime, and clear sky conditions. Moreover, it is the least sensitive close to the ground where most emissions occur (Chédin et al., 2003). Therefore, ground-based platforms are needed to complement and verify satellite data.

Ground-based detection of excess CO_2 is complicated by its quick dilution with the ~400 ppm ambient CO_2 concentration, making in situ probing at a number of points across the degassing area common (Jin et al., 2016). Most CO_2 emitters actually do not represent point sources but instead are spread out and include diffuse emissions, which complicates in situ measurements. Detecting CO_2 in situ ideally requires knowledge about vent location. Since this knowledge is often not available, emission measurements may be incomplete (Chiodini et al., 2015). An example is given by geologic CO_2 storage sites, where leak locations are unknown and CO_2 may escape via diffuse soil degassing (Patil et al., 2017). At some locations, including volcanoes or certain industrial sites, in situ measurements may even be hazardous to personnel and equipment. Moreover, some emitters may be located in remote, hard-to-reach areas.

Active optical remote sensing provides a feasible solution to these challenges. It is based on transmitting laser light that is scattered and absorbed in the atmosphere, including by gas molecules. A telescope receives the backscattered light so that its interaction with the atmosphere can be quantified. The method offers a spatially inclusive measurement with large spatial coverage, which means it accounts for all emitters, vented and diffuse, within the measurement path between the light transmitter and the backscatterer. As a single-ended technique, it does not require a receiver or reflector at the opposite end of the path. Compared with numerous in situ measurements, active remote sensing allows rapid acquisition and a safer measurement distance. By performing a scan, the gas plume distribution can be mapped or gas concentration profiles (concentration versus angle/lateral distance) measured, which can then be used to compute gas fluxes. Active remote sensors based on differential absorption LiDAR (DIAL) (Amediek et al., 2008; Aiuppa et al., 2015) and open-path spectrometers (Kameyama et al., 2009) are particularly suitable for that task.

Motivated to reduce climate impact, increase safety, or for efficiency reasons, the industry sector is placing increasing importance on ground-based sensing of fugitive CO_2, e.g., at sites for oil and gas production or geologic CO_2 injection (Naranjo and Baliga, 2012). Other than in situ sensors, common measurement techniques include fence-line monitoring, which may require numerous sensors to be installed and maintained across the facility (Thoma et al., 2011). Monitoring of fugitive CO_2 emissions at industrial sites

---

could also benefit from active remote sensing, as it is possible to scan the complete site in a few minutes with one or two sensors, yielding a quantitative picture of the emission, rather than acting as mere threshold detection.

Remote sensing instruments for gas detection at industrial and geologic sites should be as rugged, compact, and portable as possible. Technology has advanced sufficiently for instruments to be realized that fulfill these requirements (Johnson et al., 2013; Queißer et al., 2016a). While these platforms are still not mature and are subject to intense research, they are progressing rapidly toward widespread use, as recently demonstrated for urban areas (Dobler et al., 2017). Here, we demonstrate one of those instrumental platforms and its application during a test aiming to quantify a complex pattern of CO_2 emission at the Campi Flegrei (CF) volcanic caldera, Italy.
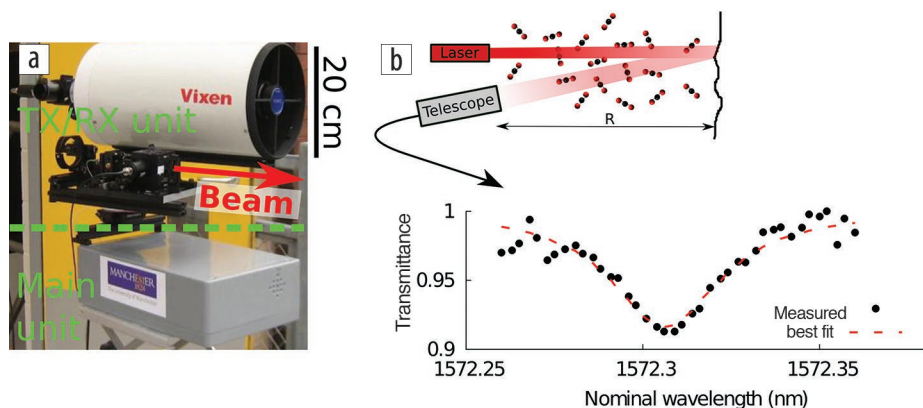

Figure 1. Working principle of LARSS. (a) A TX/RX unit (a 200 mm Cassegrain-Schmidt telescope and laser transmitter) on a step motor mount and the main unit housing opto-electronical components. (b) Basic working principle of LARSS and an example of a transmittance spectrum from the Solfatara campaign.

The open-path remote sensing spectrometer

Note that "concentration" is a rather general term. In this article, for simplicity, concentration is widely used, although it may refer to different quantities, such as "mixing ratio" or "number density." DIAL is capable of measuring range-resolved CO_2 concentrations, while open-path spectrometers acquire path-averaged (or path-integrated) CO_2 concentrations. After scanning, the former yields 2D concentration profiles and the latter yields 1D concentration profiles. However, compared with DIAL, open-path spectrometers offer a significantly higher degree of portability (handheld versus small truck), ruggedness, and user friendliness (simple measurement protocol and relatively little maintenance). For most applications, including CO_2 flux measurements, 1D concentration profiles are adequate.

Consequently, to realize a rugged and portable remote sensing tool for volcanic CO_2, the scanning open-path laser remote sensing spectrometer (LARSS) has been developed. It represents an improved and downsized version of a similar system developed in the European Research Council CO_2Volc project (Queißer et al., 2016a). The instrument and its working principle are described in detail elsewhere (Queißer et al., 2017a, 2017b). LARSS consists of a main unit and a transmitter/receiver unit (TX/RX unit, Figure 1a). The latter comprises the telescope, transmitter, and an integrating sphere for power reference measurement. Its portable mass (9 kg main unit + 6 kg TX/RX unit) allows it to be transported easily (including on commercial airliners) and set up at any kind of surface, such as on house roofs or in aircrafts (Queißer et al., 2017a).

A near infrared CO_2 absorption line (R16 transition at 1572.335 nm) is sampled at 40 wavelengths by sweeping the emission wavelength of a diode laser. The laser light is amplified, transmitted, backscattered at a topographic target (any surface, such as trees or rocks), and received by the telescope (Figure 1b). After the detected signal is digitized, the optical transmittance of the telescope's viewing path is deduced for each of the

Table 1. Meteorological data from station IPOZZUOL7 in Pisciarelli, about 1 km from the measurement site in Solfatara. WD is prevailing wind direction, WS wind speed (low and high), T air temperature, RH relative humidity, and P air pressure.

WD (°)	WS (m s−1)	T (°C)	RH (%)	P (hPa)
210	1.4–9.7	18.0	75	1005

40 wavelengths. To increase signal-to-noise ratio, per 1 s integration time 25 spectra are stacked to a single spectra to which a model absorption spectrum is fitted (Figure 1b), which is computed as follows. Using data from the HITRAN 2012 spectroscopic database (Rothman et al., 2012), air pressure and temperature are measured on site (Table 1) and the molecular absorption cross section is computed using a Lorenztian line shape. This is done for all 40 wavelengths. More details can be found in Queißer et al. (2017a). Using the fit, a best estimate of the path-averaged CO_2 concentration product Y_{CO_2} (or path amount, in ppm.m) is obtained. The path length R (range) between the instrument and the topographic target may be up to 2 km and is measured by a range-finder module. The path amount may be converted to path-averaged mixing ratios $X_{CO_2}^p$ (in ppm) after dividing by the range. 1D CO_2 concentration profiles, i.e., CO_2 concentrations versus heading angle, are attained by scanning the TX/RX unit across a degassing plume as illustrated in Figure 2. Fluxes may then be obtained by integrating over the 1D profile (Queißer et al., 2017b). LARSS currently has a path-averaged detection limit of ~10,000 ppm.m (or 12.5 ppm at 800 m path length). In other words, its measurement precision is usually between 2% and 5% of the path-averaged CO_2 mixing ratio.

2D maps of CO_2 concentration from 1D profiles

For some applications, including leakage location or hazard assessment, 2D CO_2 concentration profiles (concentration maps) may be desirable. Scanning open-path spectrometers such as LARSS provide 1D profiles only. However, if the plume is probed from different viewing angles, it is possible to obtain a 2D concentration map using matrix inversion. From an economic point of view, a realistic sales price estimate of the order of <80k Euros per LARSS unit would allow operating two or more such units simultaneously from different viewing angles to achieve that goal.
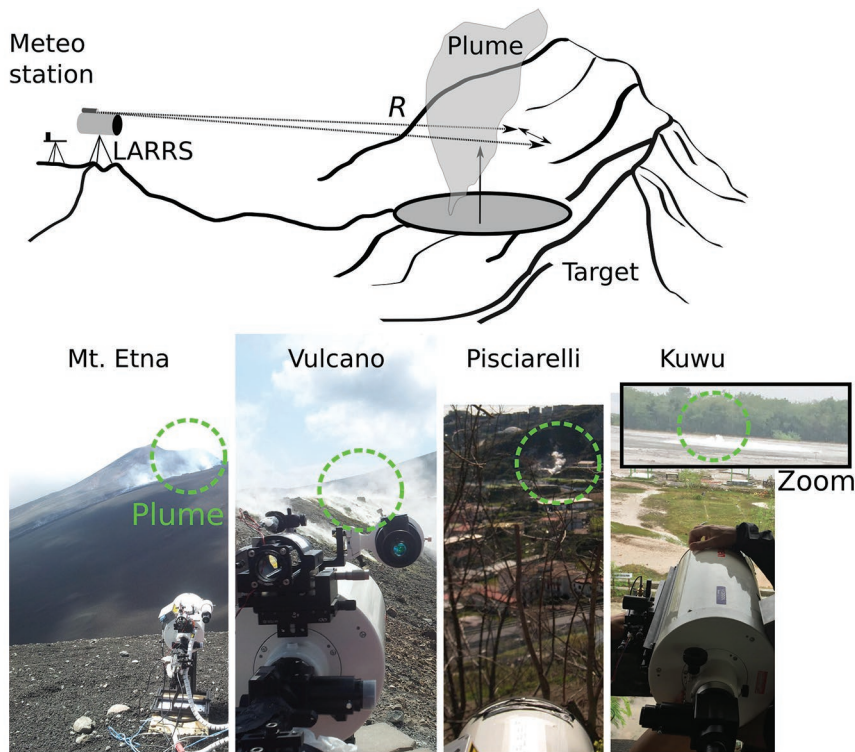
Figure 2. Field operation of LARSS. Sketch of a typical ground-based horizontal scan using a topographic target behind a plume with indicated vertical plume speed component depicted by the arrow. The photos below show LARSS measuring CO_2 plumes at different volcanic sites in Italy (first three photos) and natural CO_2 at the Bledug Kuwu mud volcano/geyser system (Java, Indonesia).

The goal is to obtain CO_2 mixing ratios X_{CO_2} at a given point (x, y). To that end, the region of interest (area bounding the scans) is divided into grid cells with length Δx (in x direction) and Δy (in Δy direction). Within a given grid cell, the associated mixing ratio is assumed uniform. The CO_2 path amount is associated with the product of a range segment and the (uniform) CO_2 mixing ratio X_{CO_2} along that range segment. For a given range and heading angle (hereafter referred to as ray) and for q grid cells traversed by the ray the corresponding governing equation can be written as

$$\sum_{i=1}^{q} r_i X_{CO_2,i} = Y_{CO_2} , \qquad (1)$$

where r_i depicts the length of the ray segment in grid cell i $\left(\sum_{i=1}^{q} r_i = R\right)$. $X_{CO_2,i}$ is the (unknown) CO_2 mixing ratio within grid cell i (in ppm). For a complete scan consisting of a number of rays (one per angle), one arrives at a system of linear equations,

$$\mathbf{Lc = a,} \qquad (2)$$

where $\mathbf{L}$ is an $m \times n$ matrix, which contains the lengths of all rays of all scans in all grid cells; n depicts the number of model grid cells and m the number of rays. For instance, the element $l_{m=211, n=9}$

would depict the length of the 211th ray in grid cell number 9. $\mathbf{c}$ is a vector of length n containing uniform X_{CO_2} per grid cell and is the desired quantity to be inverted. $\mathbf{a}$ is a vector of length m containing the measured Y_{CO_2} for each ray. More details can be found in Queißer et al. (2016b).

Since equation 2 is usually overdetermined $(m > n)$, $\mathbf{c}$ is approximated using a least-squares fitting procedure, in our case the MATLAB LSQR routine (Paige and Saunders, 1982). The algorithm iteratively seeks values for $\mathbf{c}$, which minimize the normalized misfit $\|\mathbf{a–Lc}\|$. By reshaping $\mathbf{c}$ into the measurement 2D grid, a 2D map with CO_2 mixing ratios is obtained.

The maximum model resolution given by n is limited by various factors, including ray coverage, overlap, and gas dispersion dynamics (see Queißer et al., 2016b for a detailed discussion), and so is the information that can be retrieved. It is common to apply ordinary kriging interpolation (e.g., Pedone et al., 2014), which, of course, yields a higher resolution estimate of features already included in the map, rather than increasing the actual information content (number of features in the map). The overall work flow is depicted in Figure 3.

2D maps of CO_2 concentration at Solfatara

About 12 km wide, the caldera of CF in southern Italy is among the world's most potentially destructive volcanoes. It is in a state of increased unrest (Kilburn et al., 2017; Queißer et al., 2017c) and located within the Naples urban area of approximately 3 million residents (Figure 4a). CO_2 is abundant in magmas and thus linked to volcanic processes, and CO_2 fluxes therefore provide a viable indicator to assess the hazard at CF (Chiodini et al., 2015; Cardellini et al., 2017). The crater of Solfatara, located near the center of CF, is an ideal geochemical sampling location to study the volcanic processes taking place beneath CF. Degassing at the Solfatara crater consists of diffuse soil degassing and degassing from two main vents (Bocca Nuova [BN] and Bocca Grande [BG] Figure 4b) in addition to numerous smaller vents, many of which have not yet undergone sampling (Chiodini et al., 2015). A spatially comprehensive measurement of CO_2 flux accounting for all possible CO_2 vents and diffuse degassing is therefore desirable to obtain a representative quantitative picture of CO_2 degassing, which is key for enhanced civil protection at CF.

To produce a comprehensive picture of CO_2 emissions from CF, 1D CO_2 concentration profiles were acquired with LARSS on 25 May 2017 between 11:40 and 13:10 local time. Three scans at three different positions were carried out by pivoting the step-motor-mounted TX/RX unit with 4 mrad/s (Figures 4b and 4c), corresponding to a section of roughly 1 m per measurement. A

heavy rain shower delayed the acquisition series, so the scan at position 1 was redone after the scans at position 2 and 3 were finished. The durations of the scans were 14 minutes (position 2), 10 minutes (position 3), and 14 minutes (position 1).
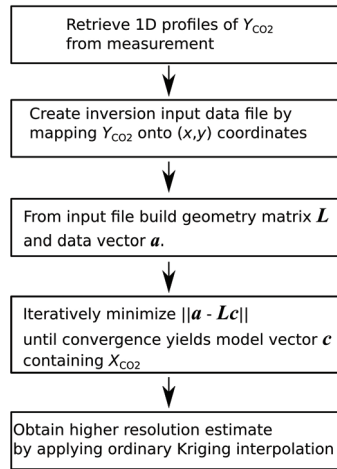

Figure 3. Scheme summarizing the main steps involved in calculation of a 2D CO_2 concentration map, starting from the field measurement.

As opposed to a permanently installed sensor, scanning gas plumes in the field is more demanding since one has limited time to carefully select an optimal point and elevation to set up the instrument. The topography of the Solfatara crater interior posed additional challenges to maintain equal scanning heights above the ground. Moreover, degassing at Solfatara takes place at different heights, including the slopes of the crater edge. Scanning the Solfatara crater interior was thus a tradeoff between capturing all sources and minimizing the effect of dispersion. Many of these challenges would also exist in an industrial or urban setting. To obtain a 2D CO_2 concentration profile that would closely resemble the actual vent and degassing source distribution prior to dispersion, the measurement paths (rays) were chosen to be as close to the ground as possible (1.5 m), which, given the heterogeneous topography of the Solfatara crater, was compromising the ray coverage at places (Figure 4c).

Synthetic test results

Before real data results are presented, the result of a synthetic test using the actual measurement geometry from the Solfatara acquisition is shown in the following. Figure 5 illustrates the retrieval of a 2D CO_2 concentration map for a synthetic CO_2 distribution, a Gaussian excess CO_2 plume adding to an ambient CO_2 mixing ratio of 420 ppm (Figure 5a) and peaking at 2100 ppm. This order of magnitude may occur at volcanic degassing sites or upon a large leakage at industrial sites (Naranjo and Baliga, 2012). Two scans probing the CO_2 plume are simulated, one from position 2 (POS 2) and one from position 3 (POS 3, Figure 5b) using the rays from two of the real scans at Solfatara. Some of the rays were discarded due to invalid data associated with them. In addition, in some places the range varies abruptly due to topographic obstacles at which light emitted by the range finder bounced back. Some of the rays were discarded due to invalid data associated with them (invalid transmittances). In addition, in some places the range varies abruptly due to topographic obstacles at which light emitted by the range finder bounced back, indicating invalid data, which were therefore also omitted. 1D concentration profiles $\mathbf{a}_{synth}$ associated with positions 2 and 3 were computed using equation 2. Figure 5c shows these profiles, which for display purposes were converted to path averaged mixing ratios $X^p_{CO_2}$, retrieved by dividing the Y_{CO_2} values by their associated ranges. Figure 5d shows the inverted 2D CO_2 concentrations $\mathbf{c}_{synth}$, and Figure 5e confronts real and inverted concentrations per grid (starting from the bottom left corner). The
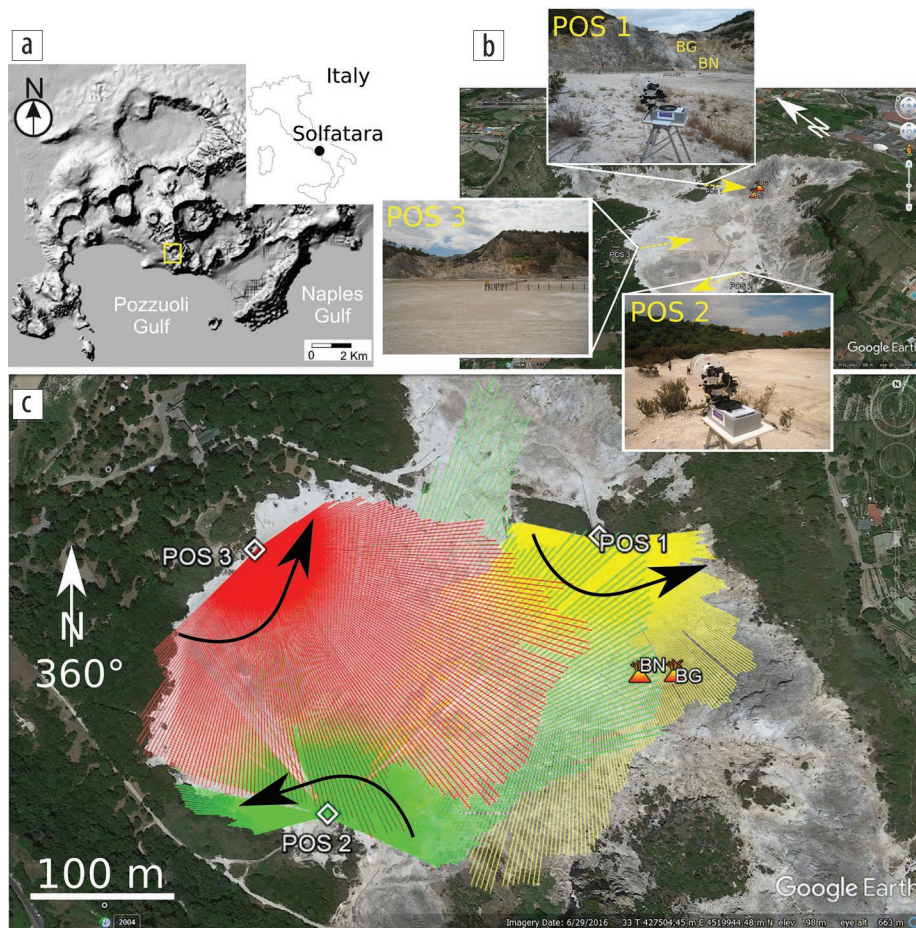

Figure 4. Measurement at Campi Flegrei, Italy. (a) Location of the Solfatara crater (yellow box). (b) 3D aerial view with measurement positions of LARSS inside the Solfatara crater and photos from the positions looking toward direction indicated by arrows. BN and BG depict the main vents Bocca Nuova and Bocca Grande. (c) Nadir aerial view showing ray coverage of scans from all three positions. Arrows depict the anticlockwise scanning direction.

concentrations are generally well recovered (normalized misfit <10^{-3}). As expected, those grids with poor or no ray coverage (especially from grid 200 onward) are associated with a relatively poor recovery of CO_2 mixing ratios.

Real data results

Figure 6 shows the three measured 1D CO_2 concentration profiles associated with the three scans (Figure 4c). Each point corresponds to 1 s integration time per angle. Since only one LARSS unit was available, the scans could not be acquired simultaneously, but instead were acquired sequentially. That means one has to assume the CO_2 distribution did not change during the 90 minutes of the acquisition ("frozen plume"). As in reality this is not the case, depending mainly on the meteorology, at some places this may lead to a skewed 2D map with respect to the real CO_2 distribution.

Discarded rays (Figure 4c) are associated with bad data, i.e., spectra that were rejected due to a bad fit. Reasons for rejection included high background noise, low absorption, or topographic obstacles. One of the chief contributions to the measurement error was in fact the fitting error. The total uncertainty of the path-averaged CO_2 mixing ratios in Figure 6 typically amounted to between 25 and 80 ppm (3% to 11% relative uncertainty).

As for the synthetic test, a 16 × 16 grid was used for the matrix inversion (grid spacing 25 and 22 m in x and y direction). The inversion result was interpolated onto a four times finer grid using ordinary kriging interpolation and is shown in Figure 7a. Anomaly A is likely an artifact since there is no ray overlap associated with that location. For reference, in situ concentrations were acquired using a LI-COR CO_2 analyzer between 11:30 and 12:30 local time (Figure 7b). The in situ values were acquired tens of minutes before or after the corresponding sections were
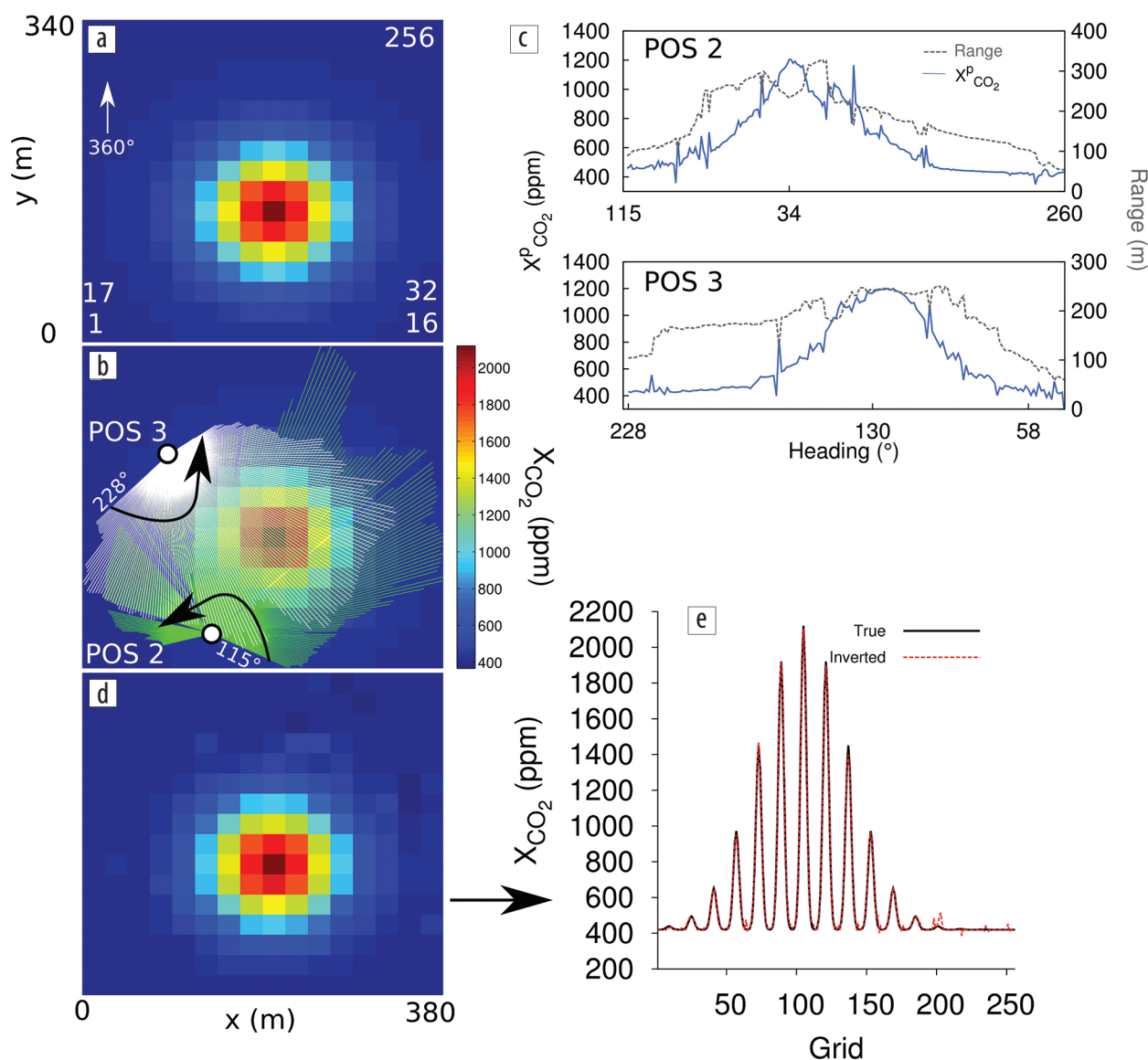

Figure 5. Synthetic tomographic inversion test using rays from POS 2 and POS 3 (Figure 4c). (a) True CO_2 concentration map with 16 × 16 grids. (b) Path length at given heading angle of scan (rays) superposed onto the true model. (c) 1D CO_2 concentration profiles, that is, path-averaged concentrations versus absolute heading angle for both instrument positions. The peak is located at 34° and 130°, respectively. The occasional spikes are a result of the finite extension of the model grids (coarseness) and/or abruptly varying path lengths. (d) Retrieved 2D map. (e) Comparison between real and retrieved model per grid. The grid numbering convention is shown in (a).

probed by LARSS, representing a snapshot at a single point and are therefore only an approximate reference for the inverted 2D concentration map. As already described earlier with the frozen plume assumption, on the scale of tens of meters the dispersion pattern is expected to change within seconds, as wind enters the crater, is deflected at the edges, and produces local eddies. The concentration pattern thus has a wavering, fluctuant shape.
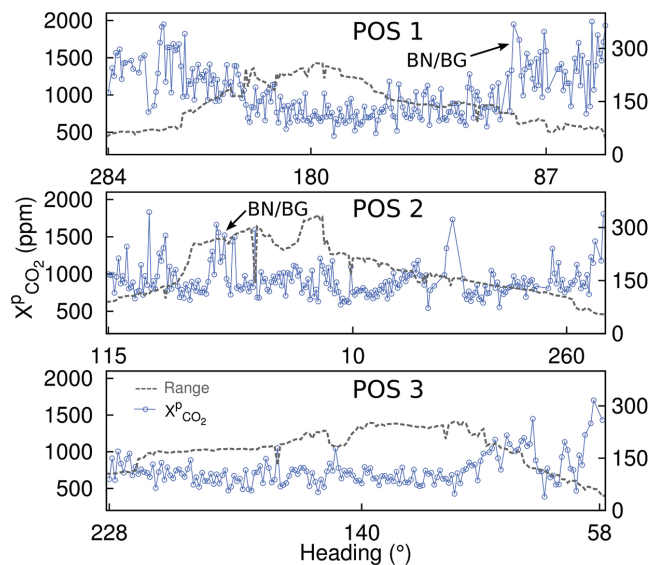

Figure 6. 1D CO_2 concentration profiles associated with positions 1, 2, and 3 in Figure 4c. BN/BG marks the heading of the Bocca Nuova and Bocca Grand main fumaroles.
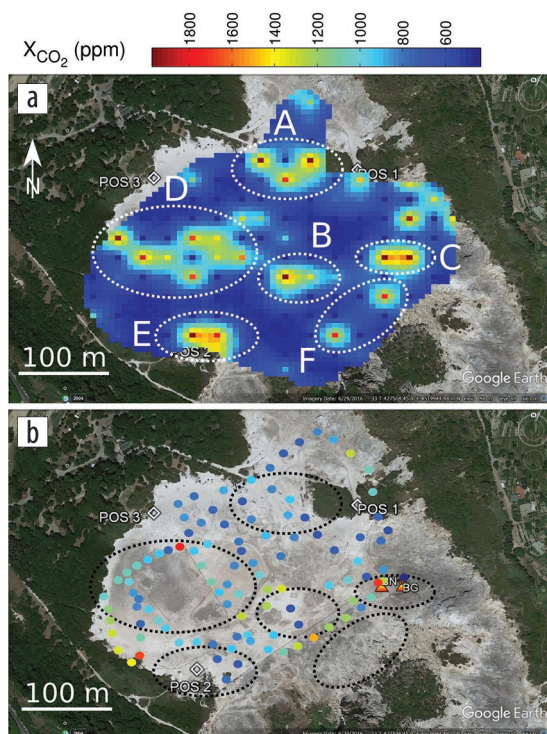

Figure 7. Real data 2D tomography of CO_2 concentration at Solfatara. (a) Inverted and interpolated (ordinary kriging) CO_2 concentration map superposed onto nadir image of Solfatara for those areas covered by the rays. (b) Map showing places and magnitude of in situ CO_2 concentrations measured with a LI-COR CO_2 analyzer.

Mismatch will thus likely be related to locally different distributions being probed by LARSS and the LI-COR.

Elevated CO_2 concentrations (around 1200 ppm) are present in the center of the crater (B, Figure 7a) and are similar to in situ measurements (Figure 7b). Both the in situ data and the tomography result indicate four zones of CO_2 concentrations surpassing 1400 ppm. One of them, marked with C, is the area near BN and BG (Figure 7a). The corresponding concentrations in the 2D map are among the highest, as expected, and are in line with an elevated in situ reading at that location. The good match for the eastern part of the crater (including BN and BG) may result from shelter provided (Figure 4b) against the southernwestern wind blowing that day (Table 1), which prevented a quick dilution or dislocation of the CO_2 anomaly. The reason may also be that strongly and permanently degassing features, such as BN and BG, better comply with the frozen plume assumption. Maximum in situ CO_2 concentrations (1803 ppm) were found in the western part near position 3, where corresponding concentrations are also present in the 2D map (zone D). Another hot spot in the 2D map, zone E, seems displaced by ~50 m toward the east with respect to the in situ values, which indicate elevated concentrations at the western edge of the region of interest. There is, however, a concentration of 1200 ppm at the associated location in the 2D map, which could be related to those prominent in situ values.

The aforementioned dispersion may partly explain why maximum in situ mixing ratios were ~1800 ppm, while LARSS detected maximum values up to ~2000 ppm (Figures 6 and 7a). The typical measurement accuracy and precision of LARSS may account for up to a difference of ~40 ppm (path averaged) in addition to the inversion error, which is of the order of 100 ppm. Moreover, while care was taken to measure at equal heights, there might have been a height difference between the laser beam of LARSS and the LI-COR of the order of 40 cm at certain places, which may well have contributed to this discrepancy as a dispersion-modeling test showed. For a given vertical column, a vertical CO_2 release at 0 m with an associated excess concentration of 1000 ppm at 0 m would decay exponentially to between 700 and 250 ppm at 1 m and to between 650 and 124 ppm at 1.5 m above ground, given various wind speeds measured on site (Table 1). In fact, the connected, elongated zone of CO_2 concentrations (F) stretching toward the southwest along the crater edge, is coherent with Figure 7b but shifted, likely because the beam path was probing at a higher level and detected a buoyant plume of CO_2, which was located about 35 m further south.

In contrast to, for instance, seismic tomography, the tomography performed here allows easy access to the region of interest and thus hard data to compare with, providing striking evidence of the nonuniqueness of the problem. During the course of testing different inversion parameters (e.g., grid number n, number of rays used) a lower normalized misfit was often associated with a 2D map that poorly recovered well-known features, such as BN and BG. Misfits were between 4% and 35%. The model the most consistent with a priori knowledge and in situ data corresponds to a relative misfit of 30%. The issue here is that the more rays are involved the more features can be recovered, but equation 2 becomes more inconsistent and so it becomes more challenging to reduce the misfit. For the future and especially for real-time

monitoring, the number of rays has to be minimized to increase consistency but be sufficiently high to allow good model recovery by adapting the measurement geometry to the particular site, which, as discussed earlier, becomes easier once the instruments are installed at a fixed location.

Conclusion

The one-sided scanning open-path laser remote sensing spectrometer LARSS provides a timely and comprehensive measurement of CO_2 concentrations; it is not a mere threshold detector, but is able to provide quantification of CO_2 fluxes and, as this exercise has demonstrated, is able to localize them. Using 1D CO_2 concentration profiles acquired with LARSS, we have successfully tested the retrieval of 2D CO_2 concentration profiles at the Solfatara crater, Italy. Solfatara is a representative example of a spatially extended, heterogeneous degassing pattern of CO_2 as it may occur in many other cases, including CO_2 storage sites or fugitive CO_2 degassing from an industrial facility. The method presented here therefore has widespread potential applications for monitoring and quantification of challenging CO_2 degassing patterns.

More refinement is needed to decrease the inversion uncertainty and increase automatization of retrieval and spatial resolution of the 2D maps. Furthermore, to increase measurement precision by at least two times, LARSS is currently being upgraded to a higher acquisition rate, which hopefully will allow it to be deployed in quantifying the more subtle urban and industrial CO_2 plumes in the near future.

Further miniaturization of LARSS toward a payload for an unmanned aerial vehicle (UAV) is considered. The main challenge here is a good tradeoff between the size/weight of the telescope and the laser power dictating the weight of the main unit. A system weighing less than 5 kg with at least 100 m measurement range is estimated to be feasible. A UAV-borne system would increase the possible number of measurement geometries. For instance, a plume could be scanned quickly in one of all three planes to account for the plume speed vector to retrieve CO_2 fluxes. **TLE**

Corresponding author: manuelqueisser@web.de

References

Aiuppa, A., L. Fiorani, S. Santoro, S. Parracino, M. Nuvoli, G. Chiodini, C. Minopoli, and G. Tamburello, 2015, New ground-based lidar enables volcanic CO_2 flux measurements: Scientific Reports, **5**, 13614, https://doi.org/10.1038/srep13614.

Amediek, A., A. Fix, M. Wirth, and G. Ehret, 2008, Development of an OPO system at 1.57 μm for integrated path DIAL measurement of atmospheric carbon dioxide: Applied Physics B, Lasers and Optics, **92**, no. 2, 295–302, https://doi.org/10.1007/s00340-008-3075-6.

Cardellini, C., G. Chiodini, F. Frondini, R. Avino, E. Bagnato, S. Caliro, M. Lelli, and A. Rosiello, 2017, Monitoring diffuse volcanic degassing during volcanic unrests: The case of Campi Flegrei (Italy): Scientific Reports, **7**, 6757, https://doi.org/10.1038/s41598-017-06941-2.

Chédin, A., R. Saunders, A. Hollingsworth, N. A. Scott, M. Matricardi, J. Etcheto, C. Clerbaux, R. Armante, and C. Crevoisier, 2003, The feasibility of monitoring CO_2 from high-resolution infrared sounders: Journal of Geophysical Research, **108**, no. D2, 4064, https://doi.org/10.1029/2001JD001443.

Chiodini, G., J. Vandemeulebrouck, S. Caliro, L. D'Auria, P. De Martino, A. Mangiacapra, and Z. Petrillo, 2015, Evidence of thermal-driven processes triggering the 2005–2014 unrest at Campi Flegrei caldera: Earth and Planetary Science Letters, **414**, 58–67, https://doi.org/10.1016/j.epsl.2015.01.012.

Dobler, J. T., T. S. Zaccheo, T. G. Pernini, N. Blume, G. Broquet, F. Vogel, M. Ramonet, et al., 2017, Demonstration of spatial greenhouse gas mapping using laser absorption spectrometers on local scales: Journal of Applied Remote Sensing, **11**, no. 1, 014002, https://doi.org/10.1117/1.JRS.11.014002.

Johnson, W., K. S. Repasky, and J. L. Carlsten, 2013, Micropulse differential absorption lidar for identification of carbon sequestration site leakage: Applied Optics, **52**, no. 13, 2994–3003, https://doi.org/10.1364/AO.52.002994.

Jin, H., T. K. Yoon, S.-H. Lee, H. Kang, J. Im, and J.-H. Park, 2016, Enhanced greenhouse gas emission from exposed sediments along a hydroelectric reservoir during an extreme drought event: Environmental Research Letters, **11**, no. 12, 124003, https://doi.org/10.1088/1748-9326/11/12/124003.

Kameyama, S., M. Imaki, Y. Hirano, S. Ueno, S. Kawakami, D. Sakaizawa, and M. Nakajima, 2009, Development of 1.6 μm continuous-wave modulation hard-target differential absorption lidar system for CO_2 sensing: Optics Letters, **34**, no. 10, 1513–1515, https://doi.org/10.1364/OL.34.001513.

Kilburn, C. R. J., G. De Natale, and S. Carlino, 2017, Progressive approach to eruption at Campi Flegrei caldera in southern Italy: Nature Communications, **8**, 15312, https://doi.org/10.1038/ncomms15312.

Naranjo, E., and S. Baliga, 2012, Early detection of combustible gas leaks using open path infrared (IR) gas detectors: SPIE Proceedings, **8366**, https://doi.org/10.1117/12.919201.

Pedone, M., A. Aiuppa, G. Giudice, F. Grassa, C. Cardellini, G. Chiodini, and M. Valenza, 2014, Volcanic CO_2 flux measurement at Campi Flegrei by tunable diode laser absorption spectroscopy: Bulletin of Volcanology, **76**, 812, https://doi.org/10.1007/s00445-014-0812-z.

Thoma, E. D., M. C. Miller, K. C. Chung, N. L. Parsons, and B. C. Shine, 2011, Facility fence-line monitoring using passive samplers: Journal of the Air & Waste Management Association, **61**, no. 8, 834–842, https://doi.org/10.3155/1047-3289.61.8.834.

Paige, C. C., and M. A. Saunders, 1982, LSQR: An algorithm for sparse linear equations and sparse least squares: ACM Transactions on Mathematical Software, **8**, no. 1, 43–71, https://doi.org/10.1145/355984.355989.

Patil, V. V., B. J. McPherson, A. Priewisch, J. Moore, and N. Moodie, 2017, Factors affecting self-sealing of geological faults due to CO_2-leakage: Greenhouse Gases: Science and Technology, **7**, no. 2, 273–294, https://doi.org/10.1002/ghg.1673.

Rothman, L. S., I. E. Gordon, Y. Babikov, A. Barbe, D. Chris Benner, P. F. Bernath, M. Birk, et al., 2013, The HITRAN 2012 molecular spectroscopic database: Journal of Quantitative Spectroscopy & Radiative Transfer, **130**, 4–50, https://doi.org/10.1016/j.jqsrt.2013.07.002.

Queißer, M., D. Granieri, and M. Burton, 2016a, A new frontier in CO_2 flux measurements using a highly portable DIAL laser system: Scientific Reports, **6**, 33834, https://doi.org/10.1038/srep33834.

Queißer, M., D. Granieri, and M. Burton, 2016b, 2-D tomography of volcanic CO_2 from scanning hard-target differential absorption lidar: The case of Solfatara, Campi Flegrei (Italy): Atmospheric Measurement Techniques, **9**, 5721–5734, https://doi.org/10.5194/amt-9-5721-2016.

Queißer, M., M. Burton, G. R. Allan, and A. Chiarugi, 2017a, Portable laser spectrometer for airborne and ground-based remote sensing of geological CO_2 emissions: Optics Letters, **42**, no. 14, 2782–2785, https://doi.org/10.1364/OL.42.002782.

Queißer, M., M. R. Burton, F. Arzilli, A. Chiarugi, G. I. Marliyani, F. Anggara, and A. Harijoko, 2017b, CO_2 flux from Javanese mud volcanism: Journal of Geophysical Research. Solid Earth, **122**, no. 6, 4191–4207, https://doi.org/10.1002/2017JB013968. PubMed

Queißer, M., D. Granieri, M. Burton, F. Arzilli, R. Avino, and A. Carandente, 2017c, Increasing CO_2 flux at Pisciarelli: Solid Earth Discuss, https://doi.org/10.5194/se-2017-70.